RESEARCH ARTICLE
SOLID EARTH: TECTONOPHYSICS

Earth and Planetary Physics
9: 1–8, 2025
doi: 10.26464/epp2025033

Evaluation of the lithospheric magnetic field mapped by the first year of MSS-1 data

S. Williams[1*], D. Gubbins[2,3], P. W. Livermore[2], and Y. Jiang[3]

[1]Institute for Marine and Antarctic Studies, University of Tasmania, Hobart, Australia;

[2]School of Earth and Environment, University of Leeds, Leeds, UK;

[3]Macau Institute of Space Technology, Macau University of Science and Technology, Macao 999078, China

Key Points:

- Evaluation of the lithospheric magnetic field mapped by the first year of MSS-1 data.
- New data compared to independent satellite observations from *Swarm* A, and tectonic models of lithospheric magnetization.
- Maps of the lithospheric field after 1 year of data reveal convergence with expected signals.

Citation: Williams, S., Gubbins, D., Livermore, P. W., and Jiang, Y. (2025). Evaluation of the lithospheric magnetic field mapped by the first year of MSS-1 data. *Earth Planet. Phys.*, *9*(3), 1–8. http://doi.org/10.26464/epp2025033

Abstract: The MSS-1 satellite began mapping Earth's magnetic field in November 2023. Here, we perform a preliminary assessment of the new information provided on Earth's lithospheric magnetic field from the first 12 months of data from MSS-1. We analyze data from the low-inclination orbital tracks of MSS-1 alongside data collected contemporaneously by the *Swarm* mission, and compare these to models for the lithospheric field from older satellite data and to predictions from models of lithospheric magnetization from tectonic constraints. We find that 1 year of data grouped into geographical bins is sufficient to produce a robust map of lithospheric anomalies. Time series analysis reveals that bins further from the equator arrive at stable values more rapidly, while equatorial regions require 9–10 months of data accumulation for stable signal recovery. The mapped data agree well with older satellite models and with predictions from a lithospheric magnetization model, with the largest mismatches suggesting that models of continental magnetization in particular require further revision. These results demonstrate the value of MSS-1's unique orbital configuration in complementing existing satellite magnetic field measurements.

Keywords: Macau Science Satellite-1; lithospheric magnetization; geomagnetism; lithospheric magnetic field

1. Introduction

Satellite missions provide a continuous mapping of the Earth's magnetic field in space and time. Among the applications of these data is the ability to map anomalies arising from variations in the magnetization of Earth's lithosphere. Maps of the lithospheric field reveal signals associated with the large-scale geological architecture of the continents (Purucker et al., 2002; Hemant and Maus, 2005), variations in the polarity of remanent magnetization of the ocean floor (Williams et al., submitted), and the nature of subduction zones at ocean margins (Williams and Gubbins, 2019).

Several previous satellite missions since the 1960s have provided data used to map the long-wavelength component of the lithospheric magnetic field (Langel and Hinze, 1998; Maus et al., 2002, 2008; Olsen et al., 2017). These missions have generally adopted near-polar orbits, achieving a complete coverage of the globe with roughly north–south track lines. The 2023 launch of the Macau Scientific Satellite-1 (MSS-1) mission (Zhang K, 2023) provides observations of Earth's magnetic field from orbits with a significantly different geometry to previous missions — the orbits are confined to lower latitudes (within around 41 degrees of the equator) so that orbital tracks contain a significant directional longitudinal component in contrast to the north-south tracks characteristic of previous missions.

Magnetic field measurements from the first eight months of MSS-1 have been used by Jiang Y et al. (2024) to derive an MSS-1 Initial Field Model (MIFM). This model is defined in spherical harmonics using additional data from the satellites of the *Swarm* mission for latitudes not covered by MSS-1. The MIFM provides a preliminary indication that MSS-1 data are able to robustly map Earth's magnetic field in space and time, including the lithospheric field to degree 40 as well as a representation of the time-varying core field.

Here, our aim is to further evaluate the signature of the lithospheric field observed by MSS-1 using a full year of data. Rather than developing a global model defined as spherical harmonics, we instead focus specifically on the orbit track data. We systematically quantify the level of agreement between track line data and existing models for the satellite magnetic field, both from earlier satel-

Correspondence to: S. Williams, simon.williams@utas.edu.au
Received 16 JAN 2025; Accepted 25 FEB 2025.
First Published online 21 MAR 2025.

lite measurements and from maps modelled from lithospheric magnetization. We additionally assess the rate of convergence between these as a function of time since the launch of MSS-1. By examining the temporal variations in data conformity, we aim to characterize the reliability and evolving precision of satellite-based mapping of the lithospheric field from different orbits.

2. Data and Methods

2.1 Satellite Data

The main data set for our study comprises the publicly available data from the MSS-1 satellite, accessed through https://mss.must.edu.mo/data.html. We use the vector magnetic field measurements sampled at 1 Hz and spanning the time period from 2/11/2023 to 31/10/2024. The data are recorded at a median altitude of 447 km, with 90% of selected data recorded within 17 km of the median altitude (Figure 1). For *Swarm* (https://earth.esa.int/eogateway/missions/swarm/data), we focus on data from *Swarm* A only, and use the 1 Hz MAGA_LR_1B product, and only consider data recorded within the same equatorial band (latitude ±41°) as the MSS-1 orbital coverage to enable comparison. Among the *Swarm* data passing the selection criteria listed below, the median altitude is 481 km, with 90% of the data from an altitude within 13 km of this median value (Figure 1).

To isolate the lithospheric field, we subtract estimates of the main internal field and external field taken from version 8.1 of the CHAOS model (Finlay et al., 2020; Kloss et al., 2024). We do not evaluate the ionospheric field component of the CHAOS-8.1 model. We derive values for the time-dependent internal field and both the far- and near-magnetospheric components of the external field for each sample point at the corresponding time, latitude, longitude and radius. We do not explicitly account for ionospheric effects, but our data selection attempts to minimize its amplitude.

Criteria for data selection are based largely on those used in previous studies of the lithospheric field, specifically the LCS-1 model (Olsen et al., 2017). We select data where the local time is within 3 hours before or after local midnight; where the sun is at least 10 degrees below the horizon; where rate of change of the RC index (Finlay et al., 2020, https://www.spacecenter.dk/files/magnetic-models/RC/) is no more than 3 nT h^{-1}; and where the geomagnetic activity *Kp* index (Matzka et al., 2021) is no more than 3. We used the python package Chaosmagpy (Kloss, 2024) to compute the local times and sun angles and evaluate the RC index at each data point.

2.2 Spherical Harmonic Models

We consider two global models for the Earth's long-wavelength lithospheric magnetic anomalies. The first is the LCS-1 model based on satellite data from the CHAMP and *Swarm* missions (the *Swarm* data from dates up to 2017). The model uses data from a range of altitudes between 480 and 250 km, from which an equivalent source representation of the lithospheric magnetization is defined. From this, Olsen et al. (2017) derive a spherical harmonic representation defined up to degree 185 which we use as a basis for our analysis.

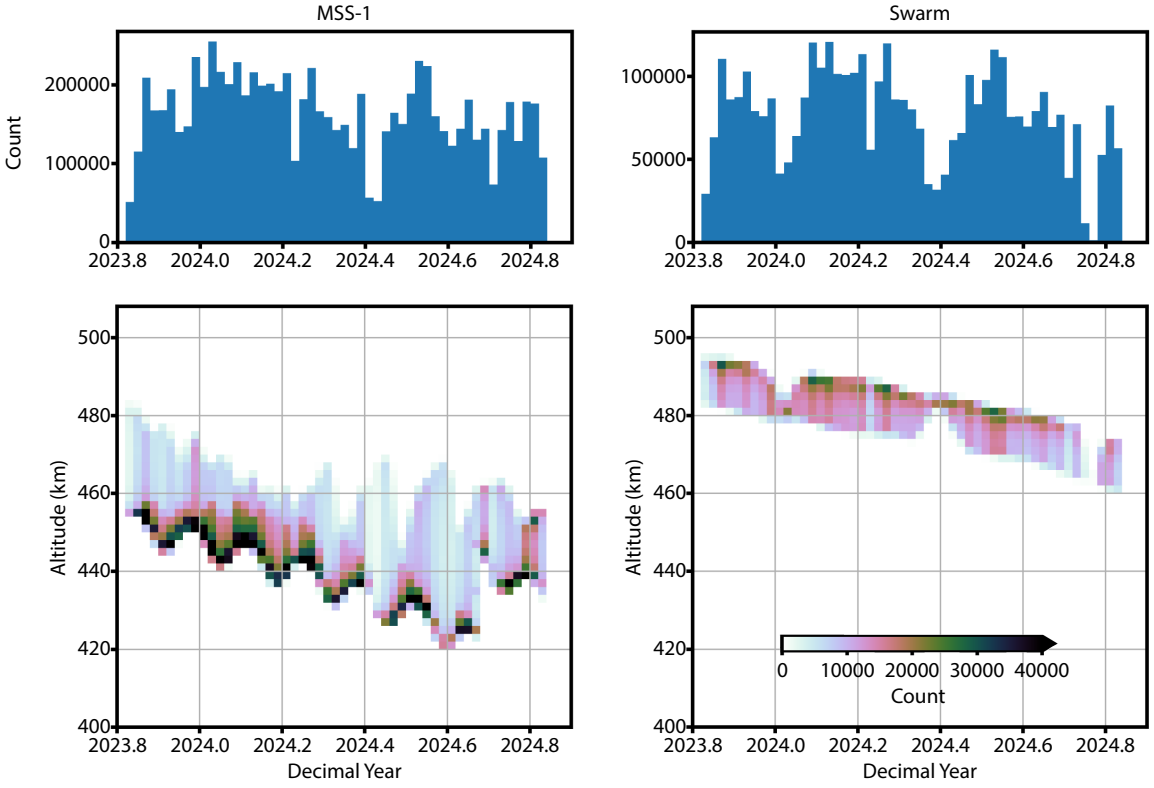

Figure 1. Summary of satellite altitudes and data count as a function of time over the 1 year study period for MSS-1 (left) and *Swarm* A (right). Note that for *Swarm* data, only data within 41 degrees of the equator are considered. Bin sizes are 0.02 years for the horizontal axis and 2 km for the vertical axis.

A second model to which we can compare the new data from MSS-1 is a forward model of the lithospheric field at satellite altitude based on a model for the lithospheric magnetization. We use the model of Williams et al. (submitted), which incorporates constraints on the lithospheric magnetization according to knowledge of Earth's plate tectonic history. Within the continental lithosphere, the model is based on regional-scale maps of continental geology (Hemant and Maus, 2005) defining for example the major cratons and orogenic belts with a resolution of 0.25 degrees. For the parts of the oceanic realm formed by seafloor spreading, the primary constraint is a model for the remanent magnetization of the oceans informed by the plate tectonic history of the ocean basins (Seton et al., 2020). Magnetization at subduction zones follows the best-fitting parameters found by Williams and Gubbins (2019).

Figure 2 shows the radial component of both the LCS-1 and lithospheric forward model, both expanded to degree 80 and plotted at an altitude of 450 km. These maps illustrate the signals expected from the lithospheric field at the present altitudes of *Swarm* and MSS-1. The strongest signals are located within the continents, such as the Bangui anomaly in Africa. Signals have generally lower amplitudes in the oceans and at satellite altitude; the only linear anomalies associated with seafloor spreading are those associated with the margins of the Cretaceous Normal Superchron (Purucker and Dyment, 2000). Between these two models, we expect recent satellite observations to conform more closely to LCS-1 than the lithospheric forward model since the changes to the lithospheric field should be negligible, and forward models show many mismatches with the older satellite observations. Nonetheless, the forward model does hold some value, showing us the extent to which the lithospheric signals are explainable by our current understanding of Earth's tectonic evolution and giving us a basis that we know is free from any unmodelled signals arising from beyond the lithosphere.

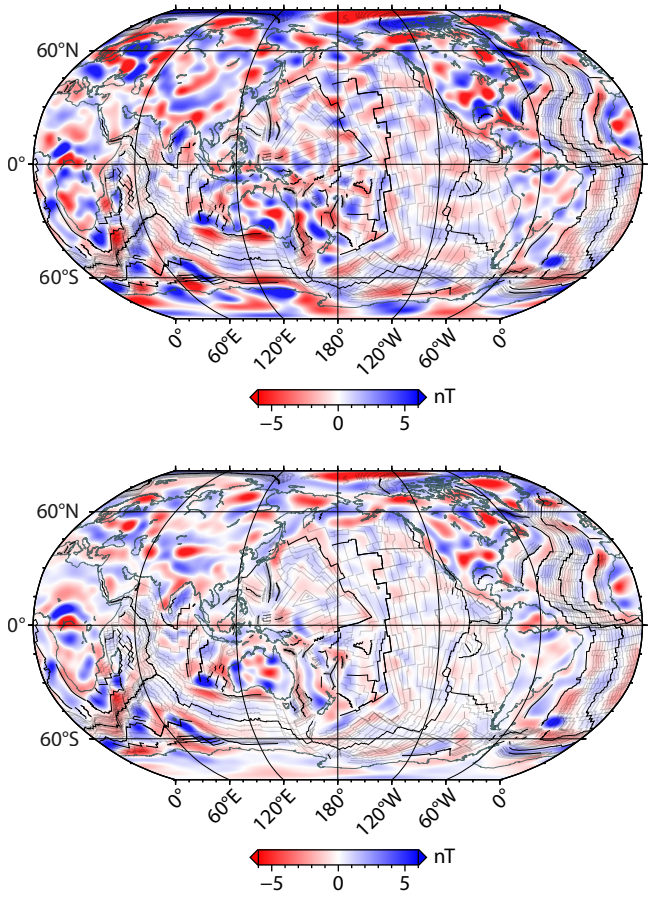

Figure 2. Radial component of the lithospheric magnetic field mapped at 450 km altitude according to the LCS-1 model of Olsen et al. (2017) (top) and the lithospheric magnetization model of Williams et al. (submitted) (bottom). Within the oceans, lines indicate seafloor age isochrons, with present day mid-ocean ridges and the young and old edges of the CNS highlighted by darker lines.

3. Results

3.1 Maps from Geographic Binning

To generate maps of the lithospheric signal from trackline data, we subdivide the dataset into geographic bins in longitude and latitude. We use the Hierarchical Equal Area isoLatitude Pixelisation (HEALPix) algorithm (Gorski et al., 1999) to derive a set of approximately equal area bins on the surface of the sphere, and assigned each data point to the coincident bin. We then use the statistics of data within each bin to support the subsequent analysis. The results are dependent on the size of the bins, so we tested different sizes and will discuss the implications of our choice. We used bootstrap resampling with replacement to determine robust statistics, using 1000 iterations and a sample fraction of 0.8 for each bin.

In Figure 3 we plot maps of radial component of the lithospheric signal from both MSS-1 and *Swarm* data from the same 1 year period. The maps are derived by evaluating the median value of all data within bins of size 1.8 degrees square (corresponding to HEALPix N_{side} = 32), with the median values then interpolated using piecewise linear interpolation on a sphere (Renka, 1997) onto a regular 1 degree grid in latitude and longitude for display purposes. Maps derived in this way neglect any difference in altitude between the different measurements. Nonetheless, these maps are able to define many of the features expected based on the maps of the radial component of field at similar altitudes from both LCS-1 and forward-modelled lithospheric magnetization (Figure 2). The strongest signals are observed within the continents, for example within southern North America, Australia, and central Africa. Within the oceans, the maps recover coherent signals related to the wide bands of continuously positive polarity remanent magnetization associated with the CNS in the Central and South Atlantic Oceans and southwest Pacific. Also recovered is a strong anomaly to the west of Australia associated with the Broken Ridge volcanic complex. Elsewhere in the Pacific and Indian Oceans, the amplitudes of the radial component are relatively subdued, consistent with expectations. However, the qualitative pattern of these weak oceanic anomalies differs considerably from those seen for LCS-1 or the forward model — for example the east–west trending linear anomaly between Madagascar and western Australia — suggesting that the currently available data are insufficient to robustly map the lithospheric signal in areas where this signal is of low amplitude.

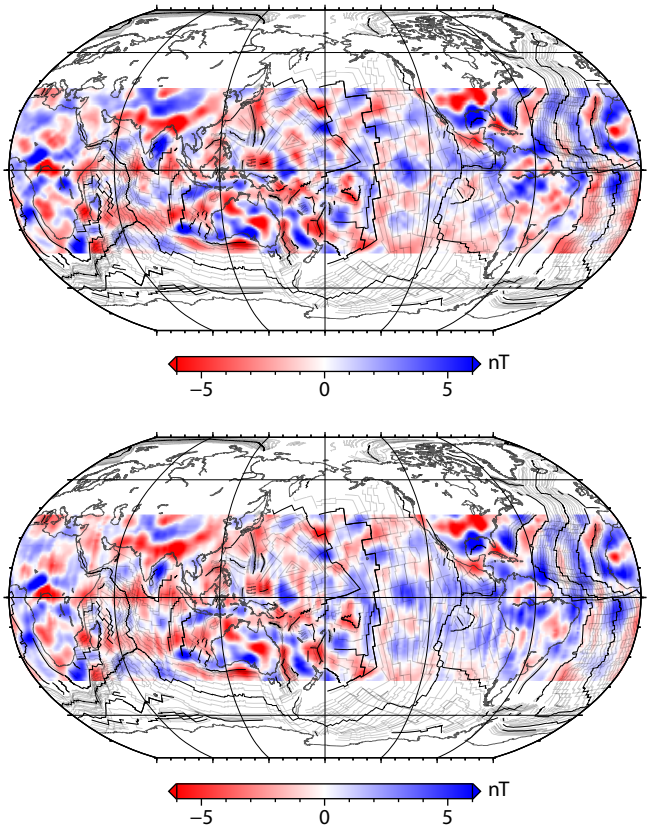

Figure 3. Maps of the radial component of lithospheric magnetic field from binned data for MSS-1 (top) and *Swarm* A (bottom) for 12 months of data. Data are from a range of altitudes which vary with time and between satellites as illustrated in Figure 1. Lines in the oceans as in Figure 2.

The maps derived from both MSS-1 and *Swarm* data exhibit short-wavelength features related to track-line noise. For MSS-1, this is mainly seen close to the equator and the noise results in spurious lineations oriented approximately NE-SW and NW-SE. For the map derived from *Swarm* across the same time period, track-line noise is oriented N-S. This fabric is visible at all longitudes, with notable examples apparent within the Arabian Peninsula, western South America and within the South Atlantic Ocean. Maps derived using a larger geographic bin size remove the track-line noise, but however reduce the level of detail in the lithospheric signal. Qualitatively, the level of track-line noise appears smaller in the maps from MSS-1 data compared with *Swarm*, likely a consequence of the greater number of tracks passing through any given bin over the same time period (Figure 4).

3.2 Model Comparisons

To quantitatively assess the fit between new satellite data and models, we evaluated the models (LCS-1 and the forward model) directly at each measurement point along track via spherical harmonic expansion. In this way, the residuals between data and models account for the varying altitude of the satellites over time. We then subdivide these residuals into geographic bins as described above, and determine the statistics of the residuals within each bin to assess the fit between data and models. These results are shown in Figure 4.

As well as mapping the fit for the full year of data we additionally determined the residuals as a function of time since the beginning of the MSS-1 data collection, to visualize the temporal trends in data-model fit throughout the first year of data collection. Figure 5 shows residuals between satellite data and the LCS-1 model as a function of time for the first 12 months of MSS-1 data collection. Again the choice of geographic bin size is arbitrary; for clarity, we choose a large bin size (HEALPix N_{side} = 4, which corresponds to approximately 15 degrees) for the plot. For each bin, the coloured points show how the median residual of the radial magnetic field within the corresponding bin using data up to time t, changes with time t increasing from left to right and plotted every 0.1 years. Time series that flatten towards the right show a convergence in the median value, while fluctuations towards the right indicate that there is insufficient data. The areas of the grey circles plotted at each bin centre scale with the number of data (after application of the data selection criteria outlined above) within each bin over the whole year. These circles illustrate the greater density of MSS-1 data further from the equator, while the Swarm data density remains relatively more uniform with latitude.

The time series in Figure 5 exhibit a few general trends. There is a clear latitudinal dependence on the slope of the time series. Bins furthest from the equator tend to produce relatively flat time series, so that the median values within these bins change relatively little after just a few months of data. By contrast, bins close to the equator show larger, more sustained changes with time across the full year of data, with many appearing to flatten out after 9–10 months. These trends are likely influenced by the larger data variances within bins closer to the equator (Figure 4), so that more data need to be accumulated for the signal-to-noise ratio to match that of bins further from the equator. Higher data density within bins further from the equator could also explain these bins more rapidly arriving at stable values. However, while the MSS-1 orbital geometries yield higher data counts further from the equator (denoted by the area of grey circles in Figure 5), the data density is more uniform in the *Swarm* data, so data density is unlikely to be the dominant factor in latitudinal trends. Latitudinal trends are also likely to arise from external sources from both the ionosphere and magnetosphere, for example associated with the equatorial electrojet (EEJ) which has a width of about 500 km and is centred on the magnetic equator. The signature of this jet is likely to remain in our processed data as its complex spatiotemporal variations are not captured by the external field model we use. The EEJ has seasonal variations which may only average to zero when considering annual or longer timeseries, and may therefore partially explain the slower convergence in equatorial bins. We do however observe differences in the time series for the two satellites: for many bins, the MSS-1 time series are steeper than the equivalent *Swarm* time series, consistent with the more rapid accumulation of data within each bin for the MSS-1 orbits regardless of specific latitude.

As a further test of level of agreement between the new data and previous models, we compared the distributions of values within each bin. To illustrate this geographically, we plot for each bin the quantile in the distribution which corresponds to a median residual of zero. For example, bins with a value of 50 correspond to a

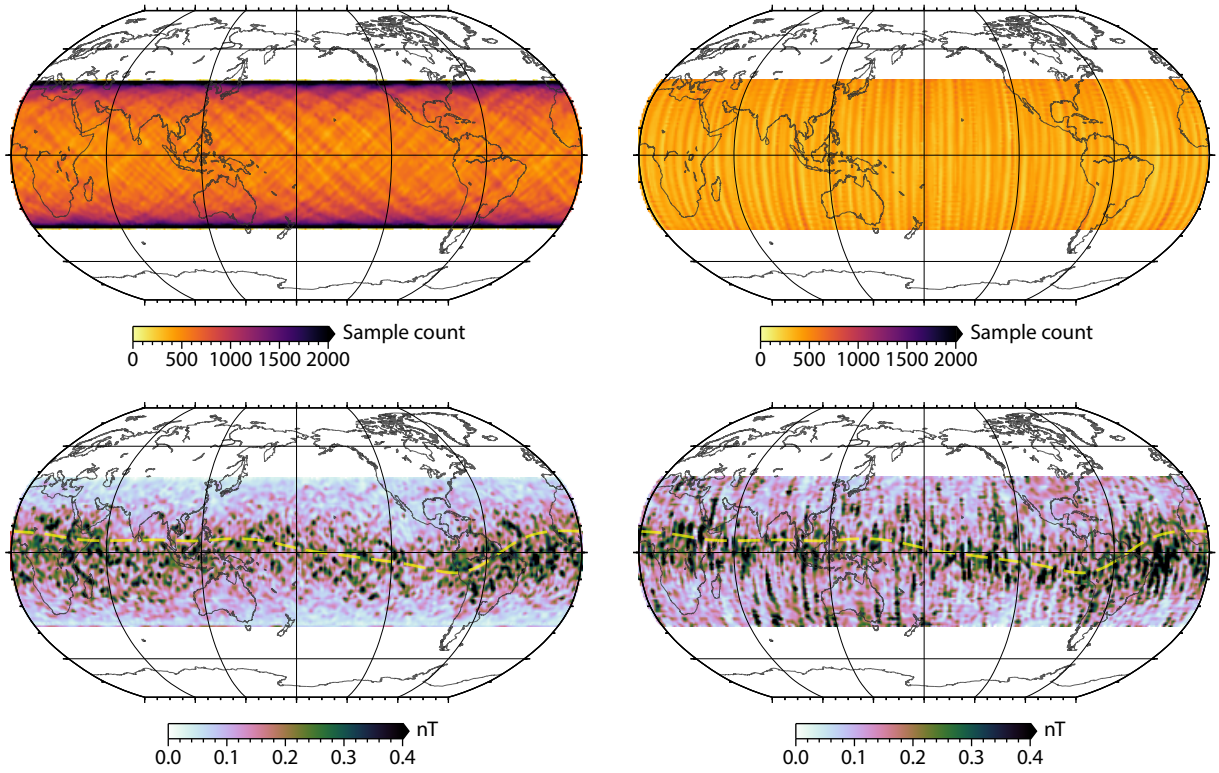

Figure 4. Maps of data density (top) and data standard deviations (bottom) for binned data for MSS-1 (left) and *Swarm* (right) for the 12 months of data used to generate the maps in Figure 3. Dashed yellow lines in lower panels indicate the magnetic equator.

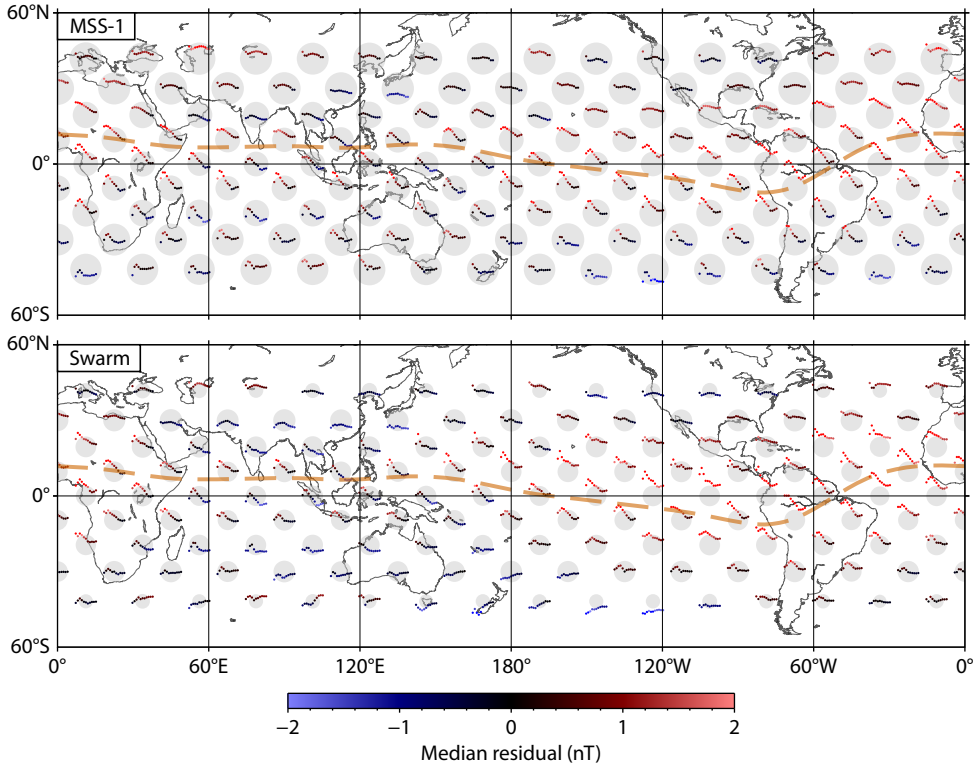

Figure 5. Time series of residuals between LCS-1 and MSS-1 and *Swarm* data, within geographic bins from November 2023 to October 2024. The area of the grey circles centred on each bin scales with the number of selected data points within the bin. The smaller coloured dots within each bin define a time-series of the median residuals for all accumulated data within the bin up to a given time. Each point represents successive times at 0.1 year intervals. The *y*-axis for each time-series defines the residual (also shown by point colour), so that zero residuals correspond to black points vertically aligned with the bin centre. The orange dashed lines show the magnetic equator which indicates the geometry of the equatorial electrojet.

median residual of zero within the bin. Conversely, bins where the distribution of the new data differs significantly from that expected from the model would yield values close to 0 (where the entire distribution of the data lies below the minimum value of the model distribution) or 100 (where data all exceed the model maximum). These values are plotted for the comparison with the LCS-1 model in Figure 6, and with the tectonics-based forward model in Figure 7. Bins for which their quantile lies outside the central 95% range (ie between 2.5% and 97.5%) are highlighted in black. Note that as with previous results, the results depend on the bin size; in these figures we use a relatively small bin size (HEALPix N_{side} = 64, corresponding to a bin size of around half a degree) to emphasize mismatches. Larger bins tend to yield values with a smaller range and fewer bins at the extremes of the 0–100 range, but the geographic patterns remain essentially the same.

Comparison between the past year of satellite observations and LCS-1 (Figure 6) reveals that, even for a bin size of 0.5 degrees, the data within the vast majority of bins lies within the central 95% of distribution of the expected values based on the LCS-1 model. For MSS-1 data 0.56% of bins contain distributions where >95% of the data lie outside the range of the expected values, while for the selected *Swarm* satellite data over the same period 2.2% of bins fall into this category. The qualitative map pattern of values is broadly similar between the two satellites, with the *Swarm* results showing a pronounced north–south fabric (which is not present for larger bin sizes) while the MSS maps show a less-pronounced along-track fabric.

The same analysis comparing satellite data against the tectonics-based forward model (Figure 7) shows a larger disagreement between the data and this model compared to the equivalent analysis for LCS-1. The proportion of bins where the data fall outside the central 95% of the values expected from the lithospheric magnetization model is 3.4% for MSS-1 data and 5.3% for the selected *Swarm* data. The qualitative map patterns show similarities with those in Figure 6, for example a concentration of poorly fitting bins located in east–west bands through southern Eurasia. Another trend in the lithospheric magnetization model comparison is poorer fit within the continents and continental margins compared to the oceans. This contrast likely reflects the different methods used to model lithospheric magnetization between these two domains. In deep ocean regions the magnetization is dominated by the magnetic stripes associated with seafloor spreading. In the continents and marginal basins, the distribution of magnetization typically reflects more complex geological histories. Furthermore, the magnetization model (Williams et al., submitted) uses a relatively up-to-date representation for the remanent magnetization associated with seafloor

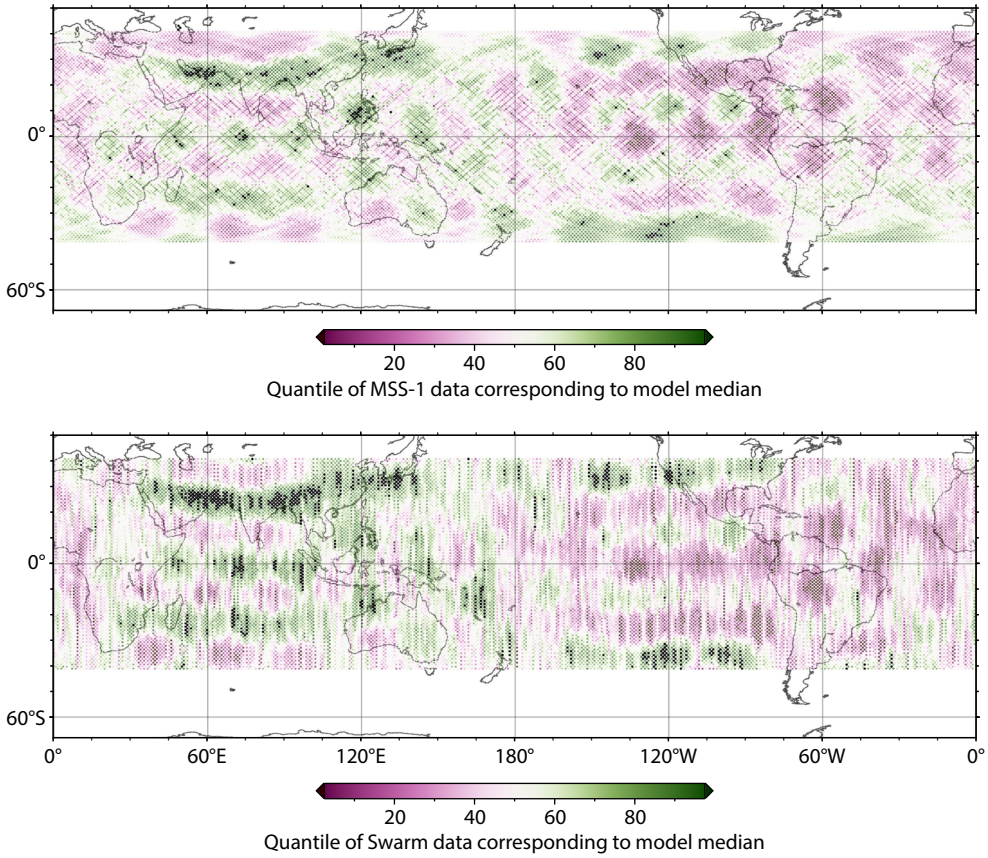

Figure 6. Maps derived from geographically-binned data showing the quantile of data distribution corresponding to a zero residual difference with the LCS-1 model. Bins where the quantile falls outside the central 95% of the distribution are highlighted as black. The upper panel shows results for selected data from the first year of MSS-1, the lower panel shows results for selected data from the *Swarm* mission across the same time period.

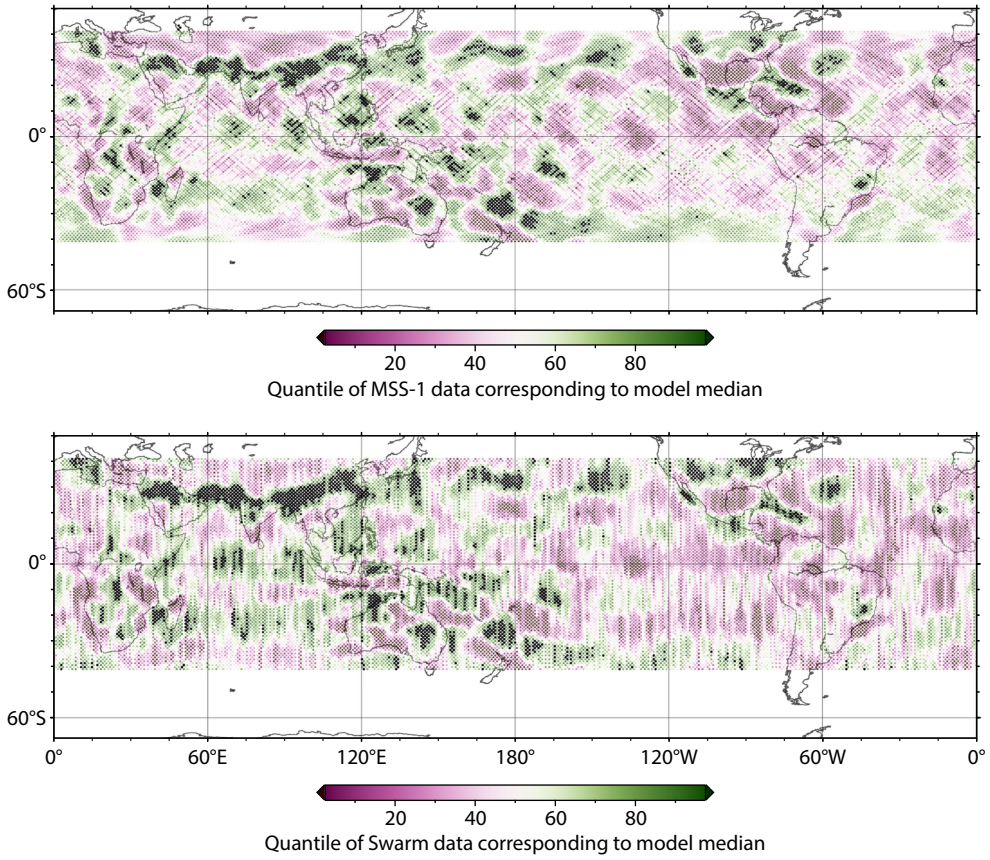

Figure 7. Maps derived from geographically-binned data showing the quantile of data distribution corresponding to a zero residual difference as in Figure 6, but here compared to the lithospheric magnetization model of (Williams et al., submitted). Bins where the quantile falls outside the central 95% of the distribution are highlighted in black. The upper panel shows results for selected data from the first year of MSS-1, the lower panel shows results for selected data from the *Swarm* mission across the same time period.

spreading (Seton et al., 2020) which shows good consistency with LCS-1 in most ocean basins, with exceptions in the northern Pacific where the tectonic model is relatively poorly constrained and the seafloor is most heavily overprinted by volcanic provinces which complicate the magnetization structure. The continental magnetization used here is unchanged from the model of Hemant and Maus (2005), which was defined on the basis of fitting the MF3 satellite magnetic model (Maus et al., 2002).

4. Discussion and Conclusions

Our analysis of the first year of MSS-1 magnetic field measurements demonstrates the satellite's capability to map the lithospheric field from its unique low-inclination orbit. MSS-1 data successfully recover major lithospheric magnetic anomalies, particularly within continental regions and areas associated with the CNS. The satellite's orbital geometry results in reduced track-line noise compared to contemporary measurements from a single *Swarm* satellite at similar altitudes, linked to the greater density of data collected by MSS in the region where the data coverages of the two missions overlap. Characteristics of the mapped lithospheric signal vary systematically with latitude, likely reflecting the difficulty in removing external field contributions. Regions further from the equator achieve stable measurements within the first few months of operation, while equatorial regions require 9–10 months of data accumulation. This pattern persists despite different data density distributions between MSS-1 and *Swarm*. Quantitative comparison with the LCS-1 model shows good agreement, with only 0.56% of geographic bins showing significant deviation for MSS-1 data compared to 2.2% for *Swarm* satellite data over the same period. Comparison with the tectonics-based forward model reveals larger discrepancies as expected (3.4% for MSS-1, 5.3% for *Swarm*), particularly in continental regions where the complex geological history makes the lithospheric magnetization more uncertain.

These results highlight the complementary nature of MSS-1's unique orbital configuration to existing satellite magnetic field measurements. The reduced track-line noise and rapid convergence at mid-latitudes suggest particular value for mapping certain regions of the lithospheric field. Future work might focus on integrating MSS-1 data with other satellite measurements to develop improved global models of the lithospheric field.

Acknowledgments

This study was supported by the Australian Research Council (grants DP200100966, FT210100557). PWL was supported as part of the *Swarm* DISC activities, funded by ESA contact no. 4000109587. Figures were created using the generic mapping tools (Wessel et al., 2019).

References

Finlay, C. C., Kloss, C., Olsen, N., Hammer, M. D., Tøffner-Clausen, L., Grayver, A., and Kuvshinov, A. (2020). The CHAOS-7 geomagnetic field model and observed changes in the south Atlantic anomaly. *Earth Planets Space*, *72*(1), 156. https://doi.org/10.1186/s40623-020-01252-9

Gorski, K. M., Wandelt, B. D., Hansen, F. K., Hivon, E., and Banday, A. J. (1999). The HEALPix primer. *arXiv*, astro-ph/9905275. https://doi.org/10.48550/arXiv.astro-ph/9905275

Hemant, K., and Maus, S. (2005). Geological modeling of the new CHAMP magnetic anomaly maps using a geographical information system technique. *J. Geophys. Res.: Solid Earth*, *110*(B12), B12103. https://doi.org/10.1029/2005JB003837

Jiang, Y., Finlay, C. C., Olsen, N., Tøffner-Clausen, L., Yan, Q., and Zhang, K. K. (2024). Macau Scientific Satellite-1 initial magnetic field model. *Geophys. Res. Lett.*, *51*(22), e2024GL112305. https://doi.org/10.1029/2024GL112305

Kloss, C. (2024). Ancklo/chaosmagpy: Chaosmagpy v0.14. Zenodo. https://doi.org/10.5281/zenodo.12200898

Kloss, C., Finlay, C. C., Olsen, N., Tøffner-Clausen, L., Gillet, N., and Grayver, A. (2024). CHAOS-8 geomagnetic field model. Zenodo. https://doi.org/10.5281/zenodo.13950013

Langel, R. A., and Hinze, W. J. (1998). *The Magnetic Field of the Earth's Lithosphere: The Satellite Perspective*. Cambridge: Cambridge University Press.

Matzka, J., Stolle, C., Yamazaki, Y., Bronkalla, O., and Morschhauser, A. (2021). The geomagnetic *Kp* index and derived indices of geomagnetic activity. *Space Weather*, *19*(5), e2020SW002641. https://doi.org/10.1029/2020SW002641

Maus, S., Rother, M., Holme, R., Lühr, H., Olsen, N., and Haak, V. (2002). First scalar magnetic anomaly map from CHAMP satellite data indicates weak lithospheric field. *Geophys. Res. Lett.*, *29*(14), 1702. https://doi.org/10.1029/2001GL013685

Maus, S., Yin, F., Lühr, H., Manoj, C., Rother, M., Rauberg, J., Michaelis, I., Stolle, C., and Müller, R. (2008). Resolution of direction of oceanic magnetic lineations by the sixth-generation lithospheric magnetic field model from CHAMP satellite magnetic measurements. *Geochem. Geophys. Geosyst.*, *9*(7), Q07021. https://doi.org/10.1029/2008GC001949

Olsen, N., Ravat, D., Finlay, C. C., and Kother, L. K. (2017). LCS-1: a high-resolution global model of the lithospheric magnetic field derived from CHAMP and *Swarm* satellite observations. *Geophys. J. Int.*, *211*(3), 1461–1477. https://doi.org/10.1093/gji/ggx381

Purucker, M. E., and Dyment, J. (2000). Satellite magnetic anomalies related to seafloor spreading in the South Atlantic Ocean. *Geophys. Res. Lett.*, *7*(17), 2765–2768. https://doi.org/10.1029/1999GL008437

Purucker, M. E., Langlais, B., Olsen, N., Hulot, G., and Mandea, M. (2002). The southern edge of cratonic North America: Evidence from new satellite magnetometer observations. *Geophys. Res. Lett.*, *29*(15), 8000. https://doi.org/10.1029/2001GL013645

Renka, R. J. (1997). Algorithm 773: SSRFPACK: interpolation of scattered data on the surface of a sphere with a surface under tension. *ACM Trans. Mathemat. Softw.*, *23*(3), 435–442. https://doi.org/10.1145/275323.27533

Seton, M., Müller, R. D., Zahirovic, S., Williams, S., Wright, N. M., Cannon, J., Whittaker, J. M., Matthews, K. J., and McGirr, R. (2020). A global data set of present-day oceanic crustal age and seafloor spreading parameters. *Geochem. Geophys. Geosyst.*, *21*(10), e2020GC009214. https://doi.org/10.1029/2020GC009214

Wessel, P., Luis, J. F., Uieda, L. L., Scharroo, R., Wobbe, F., Smith, W. H. F., and Tian, D. (2019). The generic mapping tools version 6. *Geochem. Geophys. Geosyst.*, *20*(11), 5556–5564. https://doi.org/10.1029/2019GC008515

Williams, S., Gubbins, D., Seton, M., and Whittaker, J. (submitted). Magnetization of oceanic lithosphere from modelling of satellite observations. *J. Geophys. Res.: Solid Earth*.

Williams, S., and Gubbins, D. (2019). Origin of long-wavelength magnetic anomalies at subduction zones. *J. Geophys. Res.: Solid Earth*, *124*(9), 9457–9473. https://doi.org/10.1029/2019JB017479

Zhang, K. (2023). A novel geomagnetic satellite constellation: Science and applications. *Earth Planet. Phys.*, *7*(1), 4–21. https://doi.org/10.26464/epp2023019